Development of a polarization resolved spectroscopic diagnostic for measurements of the vector magnetic field in the Caltech coaxial magnetized plasma jet experiment

T. Shikama[a] and P. M. Bellan
California Institute of Technology, Pasadena, California 91125, USA

(Received 28 November 2012; accepted 11 February 2013; published online 28 February 2013)

In the Caltech coaxial magnetized plasma jet experiment, fundamental studies are carried out relevant to spheromak formation, astrophysical jet formation/propagation, solar coronal physics, and the general behavior of twisted magnetic flux tubes that intercept a boundary. In order to measure the spatial profile of the magnetic field vector for understanding the underlying physics governing the dynamical behavior, a non-perturbing visible emission spectroscopic method is implemented to observe the Zeeman splitting in emission spectra. We have designed and constructed a polarization-resolving optical system that can simultaneously detect the left- and right-circularly polarized emission. The system is applied to singly ionized nitrogen spectral lines. The magnetic field strength is measured with a precision of about ±13 mT. The radial profiles of the azimuthal and axial vector magnetic field components are resolved by using an inversion method. © *2013 American Institute of Physics*. [http://dx.doi.org/10.1063/1.4793403]

I. INTRODUCTION

Measurements of the magnetic field strength in current-carrying magnetically confined plasmas are necessary for understanding the underlying physics governing the dynamical behavior. Such measurements are useful in the Caltech coaxial magnetized plasma gun,[1,2] an experiment used for fundamental studies relevant to spheromak formation, astrophysical jet formation/propagation, solar coronal physics, and the general behavior of twisted magnetic flux tubes that intercept a boundary. In order to measure the field strength in the experiment, a non-perturbing spectroscopic method was implemented to observe the Zeeman splitting in emission spectra.

The magnetic field strength inside the plasma is detectable from the wavelength shift of the emission spectral line induced by the Zeeman effect. In the case that the wavelength shift is smaller than the broadening of the spectral line, polarization resolving techniques have been adopted. Previously reported applications of such techniques to laboratory plasmas by means of passive emission spectroscopy can be found in Refs. 3–7. We present here a polarization-separating optical system and its application to the Caltech plasma experiment. The main features distinguishing our results from previously reported investigations are the spatial resolution of the measurements, mitigation of the large Stark broadening, and evaluation of the vector magnetic field and its spatial profile. For the first feature, the Caltech experiment requires a spatial resolution of ∼ a few mm; the optical system satisfies this requirement. The second feature was achieved by observing singly ionized nitrogen spectral lines which are relatively insensitive to the Stark broadening. Finally, an inversion method was implemented for the third feature.

[a]Permanent address: Department of Mechanical Engineering and Science, Graduate School of Engineering, Kyoto University, Kyoto 615-8540, Japan.

II. THE STARK AND ZEEMAN EFFECTS ON NITROGEN IONIC SPECTRA

The Caltech coaxial plasma gun generates a plasma with an electron density up to 10^{23} m^{-3}. Spectral line shapes from this dense plasma could be significantly affected by the Stark broadening and shift induced by the electric microfield in the plasma. In order to minimize these effects, we observed spectral lines from singly ionized nitrogen (NII) because these lines are relatively insensitive to the Stark effect compared to hydrogen-like atomic or ionic lines. The Stark broadening and shift for NII lines under the present experimental condition are proportional to the electron density.[8]

In our experiments, the magnetic field strength is smaller than 1 T. The Zeeman effect[9] on NII lines under this field strength can be approximated as the weak-field limit. The shift of the transition energy between the upper and lower magnetic sublevels is expressed neglecting the effect of the nuclear spin as

$$\Delta E_B = \mu_B B(g_J' M' - g_J M), \tag{1}$$

where μ_B is the Bohr magneton, B is the external magnetic field strength, g_J is Lande's g-factor, M is the magnetic quantum number, and the variables with prime denote those belong to the upper state. The transitions with $\Delta M = M - M' = 0$ are called the π components, while those with $\Delta M = \pm 1$ are called the σ components. The corresponding wavelength shift to Eq. (1) is expressed as

$$\Delta\lambda_B \simeq -\frac{\lambda_0^2}{hc}\Delta E_B, \tag{2}$$

where λ_0 is the unperturbed wavelength, h is Planck's constant, and c is the velocity of light. The field strength can be deduced from the wavelength shift of the σ components. For electric dipole radiation, the π and σ radiation can be described by the radiation emitted from the classical electric

dipoles oscillating in the magnetic field direction and those rotating in the left/right circular direction in a plane perpendicular to the magnetic field, respectively. Here we define the left- and right-circular polarizations from the viewpoint of the observer. If one observes the emission parallel to the magnetic field, the σ components are distinguishable by observing the right ($\Delta M = -1$) and left ($\Delta M = +1$) circularly polarized light. The σ components with $\Delta M = -1$ and $+1$ are denoted as the σ^+ and σ^- components, respectively. If observation is in a direction anti-parallel to the field, the polarizations of the σ^+ and σ^- components interchange.

One can see from Eq. (2) that for transitions which have given upper and lower state electronic configurations, the wavelength shift is approximately proportional to λ_0^2. Thus in order to maximize the wavelength shift by the Zeeman effect, we have chosen three adjacent spectral lines near the 500 nm upper wavelength limit of our spectrometer:

(i) 498.737 nm : $2s^2 2p3p\ ^3S_1 - 2s^2 2p3d\ ^3P_0^\circ$

(ii) 499.124 nm : $2s2p^2(^4P)3s\ ^5P_1 - 2s2p^2(^4P)3p\ ^5P_2^\circ$

(iii) 499.437 nm : $2s^2 2p3p\ ^3S_1 - 2s^2 2p3d\ ^3P_1^\circ$.

The magnitudes of the Stark broadening and shift for these spectral lines were taken from Ref. 8 and are listed in Table I. The shapes of the π and σ components of these spectral lines taking into account the relative transition intensities between the magnetic sublevels were calculated by quantum mechanical perturbation theory. The details of the calculation procedure can be found in Refs. 10 and 11. The procedure is applicable to nitrogen ionic lines (i)–(iii) since for these lines the coupling of the angular momenta is well represented by the LS coupling.[12,13] After convolution of the instrumental function, the peak wavelength shifts of the $\sigma^\pm$ components from the unperturbed wavelengths are proportional to the magnetic field strength. The shifts of the π components from the unperturbed wavelengths are negligibly small. Coefficients of the peak wavelength shift for the $\sigma^\pm$ components are shown in Table I.

We note from Ref. 14 that spectral line (iii) is superposed by another line (iv) 499.436 nm : $2s2p^2(^4P)3s\ ^5P_2 - 2s2p^2(^4P)3p\ ^5P_3^\circ$. Our spectroscopy system cannot resolve these lines. If we assume the statistical population distribution in the fine-structure levels, the emission intensity of spectral line (iv), which is proportional to $(2J' + 1)A_{J'J}$, where J is the total angular momentum quantum number and $A_{J'J}$ is the spontaneous emission coefficient, should be comparable to that of (ii). From the observed spectra (Figure 3 and spectra on the other viewing chords), it was estimated that the relative intensity of spectral line (iv) to that of (iii) should be smaller than 30%. The Zeeman shift of the superposed spectral line with an intensity ratio of 30% was then calculated under magnetic field strengths smaller than 1 T to estimate the variation from that of spectral line (iii). The difference in the magnitude of the Zeeman shift is less than 3% and negligible if we neglect the Stark shift of spectral line (iv). This is because the coefficient of the Zeeman shift of spectral line (iv) is 17.4 pm/T and smaller than that of spectral line (iii).

III. EXPERIMENTAL SETUP

A. Polarization-separating optical system

We designed a polarization-separating optical system which spatially resolves the left- and right-circularly polarized emission and then transfers this polarization resolved light to a high-resolution spectrometer with gated intensified charge-coupled device (ICCD) detector. A schematic drawing of the system is shown in Figure 1. It consists of a quartz lens (Sigma-Koki plano-convex lens; $f = 60$ mm), an achromatic $\lambda/4$ plate optimized for operation at 500 nm (Edmund Optics NT48-497), a beam-splitting Glan-Thompson prism (Halbo Optics PTBS10), and a custom-built 32-element optical fiber bundle (Mitsubishi Cable Industries ST230D; core and cladding diameters are 230 and 250 μm, respectively). Left- and right-circularly polarized light from the plasma corresponding to the Zeeman-split σ components is converted into the orthogonal linearly polarized light by the wave plate and then spatially separated into the ordinary (vertically polarized in the figure) and extraordinary (horizontally polarized) light by the Glan-Thompson prism. The separated light is transferred via the fiber bundle which consists of two 16-element sets of vertically aligned fibers to a Czerny-Turner type spectrometer (Jobin-Yvon Horiba 1000 M; $f = 1$ m, 3600 grooves/mm grating). The bundle is arranged so that the initially left- and right-hand light is carried on the odd- and even-numbered fibers, respectively. The spectra are recorded by an ICCD detector (Andor DH520-25F-03; 800 × 250 active pixels, 26 μm square pixel). Because of the limitation of the detector height, only signals from 26 out of the 32 fibers are simultaneously recordable. Spectra for the 26 fiber elements were obtained by binning of the ICCD image in a direction perpendicular to the wavelength dispersion direction; 9 pixels were summed for each fiber element. The change of the $\lambda/4$ plate retardance due to the oblique incidence of light is reported to be less than 1% for $\pm 3^\circ$. Although the present system has the maximum angle of about $\pm 6^\circ$, considering the variation of the incidence angle within a cone of the light path, the change of the retardance may be negligible.

The reciprocal linear dispersion of the spectrometer and ICCD was measured by using pairs of mercury atomic spectral lines simultaneously recordable within the same ICCD frame. The measured data were fitted by the theoretical curve[15] with f and δ as fitting parameters, where f is the focal length of the spectrometer and δ is the angle between the incident or diffracted light of the grating and the spectrometer axis, the bisector of the incident and diffracted light. Our spectrometer has a diffraction order of unity and a 3600 grooves/mm grating. The determined parameters are $f = 1.027 \pm 0.002$ m and $\delta = 5.894^\circ \pm 0.105^\circ$. The reciprocal linear dispersion calculated from this theoretical curve is 3.6 pm/pixel at 500 nm. The standard deviation of the dispersion calculated from those of f and δ is negligibly small. The instrumental function was measured by using a mercury atomic spectral line HgI 491.607 nm : $5d^{10}6s6p\ ^1P_1^\circ - 5d^{10}6s8s\ ^1S_0$. The line profile was fitted by the Voigt function. The instrumental function has Gaussian and Lorentzian widths of about 17 and 6 pm, respectively.

TABLE I. The Stark[8] and Zeeman effects on the NII spectral lines. (i) 498.737 nm : $2s^2 2p3p\ ^3S_1$-$2s^2 2p3d\ ^3P^\circ_0$, (ii) 499.124 nm : $2s2p^2(^4P)3s\ ^5P_1$-$2s2p^2(^4P)3p\ ^5P^\circ_2$, and (iii) 499.437 nm : $2s^2 2p3p\ ^3S_1$-$2s^2 2p3d\ ^3P^\circ_1$. The Stark broadening is the FWHM of the spectral line. The Zeeman shift is the magnitude of the peak wavelength shift for the $\sigma^\pm$ components from the unperturbed wavelength.

Transition	(i) 498.737 nm	(ii) 499.124 nm	(iii) 499.437 nm
Stark broadening ($\times 10^{-23}$ pm/m^{-3})	49.8	24.4	44.1
Stark shift ($\times 10^{-23}$ pm/m^{-3})		−4.2	
Zeeman shift (pm/T)	23.2	17.4	20.4

The shapes of the viewing spots at the plasma center, where the distance from the objective lens is 950 mm, were measured by injecting 532 nm wavelength light from a diode-pumped solid-state laser into the optical fiber at the spectrometer side. The viewing spot of the ordinary ray is about 3.7 mm diameter circle. In contrast, that of the extraordinary ray is a horizontally elongated ellipse with major and minor axes of about 10 and 3.7 mm, respectively. This is because in the Glan-Thompson prism the refractive indices in the meridional and sagittal directions are different for the extraordinary ray. The centers of the ordinary and extraordinary ray viewing spots were made to coincide by adjusting the bifurcated end positions of the optical fiber. The relative sensitivity of each fiber channel was calibrated by using the above mentioned mercury atomic spectral line reflected by a diffuse reflectance plate (Labsphere SRS-99-020) so as to provide uniform intensity light to all the fiber elements. The relative wavelength among the 26 spectra was calibrated by using a hydrogen molecular spectral line existing near the NII spectral lines. The transition term and absolute wavelength of the molecular line were not identified since only the relative wavelength calibration between the ordinary and extraordinary spectra is important in the present measurements. The precision of the calibrated wavelength difference between the ordinary and extraordinary spectra is about ±0.1 pixel.

B. Caltech coaxial magnetized plasma gun experiment

The measurements were carried out using the Caltech coaxial magnetized plasma gun (Figure 2). Details of the plasma gun and its sequence of operation can be found elsewhere.[2,16,17] In the present experiment, the peak discharge voltage was set to 5 kV and peak current was 110 kA. Nitrogen was used as the working gas. Typical electron and ion temperatures (T_e and T_i) are about 3 eV and electron density (n_e) is 10^{21}–10^{23} m^{-3}. The magnetic field consists of a poloidal component resulting from stretched externally imposed bias magnetic flux and a toroidal component generated by the poloidal plasma current from the gun electrodes. The direction of the poloidal field could be reversed by switching the polarity of the coil current. The direction of the toroidal field was fixed; the plasma current flows from the outer (anode) to center (cathode) gun electrodes. In order to have an axisymmetric plasma, the discharge regime with low λ_{gun} ($= \mu_0 I_{gun}/\psi_{gun}{}^2$) for which a central plasma column forms was adopted, where I_{gun} is the total gun current and ψ_{gun} is the total magnetic flux.

The optical system was installed in front of a 203 mm diameter viewport (borosilicate glass) closest to the plasma gun. The axial displacement of the window center from the gun electrodes was 295 mm. The viewing chord was aligned in a direction 79° from the vacuum chamber axis. The difference in the window transmittances for the s- and p-polarized light by oblique observation is negligibly small. The point where viewing chords intersect the plasma center is 950 mm from the objective lens and 70 mm from the surface of the gun electrodes. The total height of the region observed by 13 chords is about 48 mm. The spectrum was recorded 7 μs after the onset of the discharge with an ICCD exposure of 1 μs. The plasma is fully ionized, and almost all visible emission originates from singly ionized nitrogen. The plasma jet propagates about 3 cm during the exposure.[18] Since the plasma under consideration is a stretched jet, and the visible image taken by a fast camera at the timing of the exposure is axially uniform in a spatial scale of several cm around the viewing point, the effect of the plasma displacement is negligible in the present measurements.

IV. RESULTS

A measurement was carried out in a discharge with the poloidal field directed toward the gun electrodes in the vicinity of the chamber axis. For reference, this is called the

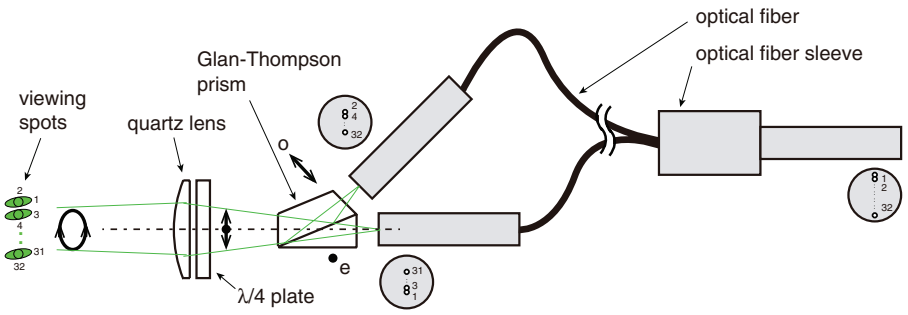

FIG. 1. A schematic drawing of the polarization separating optical system. o and e stand for the ordinary and extraordinary light, respectively.

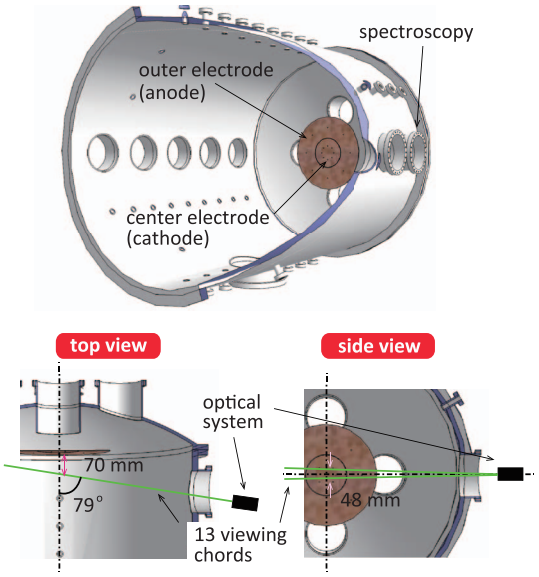

FIG. 2. Schematic drawings of the vacuum chamber and viewing chords. y is defined as the height from the mid-plane.

normal poloidal field direction corresponding to positive magnetic helicity. A spectrum observed on a viewing chord near the center of the plasma is shown in Figure 3. The spectrum consists of the line-integrated emission along the viewing chord. We evaluate the "apparent" peak wavelength shifts by the Zeeman effect in the line-integrated spectral lines and then resolve the local magnetic field vectors by an inversion method described in Sec. IV A. In the following discussions, we use the bar, e.g., $\overline{B}$, for variables measured from the line-integrated spectra. Otherwise variables represent quantities at localized spatial positions.

As can be seen in Figure 3, the spectral lines have significant Stark broadening and as a result their pedestals overlap. The apparent peak wavelength differences between the ordinary and extraordinary spectral lines are smaller than 2 pixels.

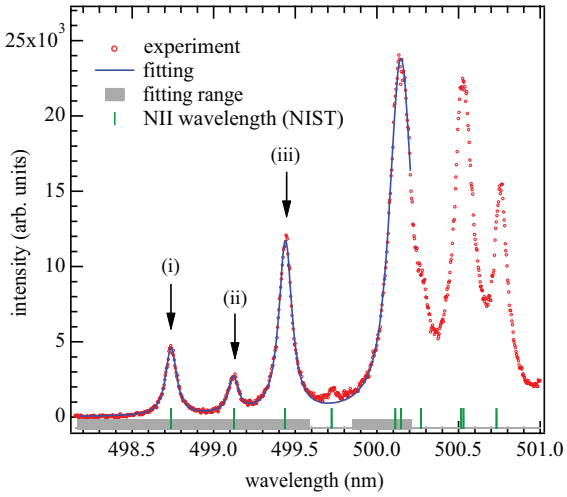

FIG. 3. A spectrum observed on a viewing chord near the plasma center. The open circles denote the experimental data and line denotes the fitting result. On the abscissa, fitting wavelength ranges are indicated by the thick gray lines. The wavelengths of NII transitions[14] are denoted by the vertical ticks.

In order to measure these small splittings accurately, a fitting procedure taking into account the overlapping of the pedestals was adopted. In this procedure, spectral lines (i), (ii), (iii), and a nearby peak at 500.15 nm were fitted simultaneously. The fitting function is expressed as

$$f(\lambda) = f_0 + \sum_{n=1}^{4} A_n L_V(w_{Gn}, w_{Ln}, \lambda_{pn}; \lambda), \qquad (3)$$

where f_0 and A_n are the constants and $L_V(w_{Gn}, w_{Ln}, \lambda_{pn}; \lambda)$ is the Voigt function. For the arguments of the Voigt function, w_G and w_L represent the FWHMs of the Gaussian and Lorentzian widths, respectively, and λ_p is the peak wavelength. The Stark, Doppler, and instrumental broadenings are considered. In our plasma, the Doppler broadening is smaller by several times than the Stark broadening, and so difficult to distinguish. A uniform T_i of 3 eV over the whole plasma radius was assumed. The value is based on an assumption $T_e = T_i$ and previously measured $T_e \simeq 3$ eV[18] from a line-integrated spectrum at the plasma center with local thermodynamic equilibrium (LTE) assumed. The fitting was carried out in a wavelength range 498.2–500.2 nm. A wavelength range 499.60–499.85 nm was excluded because the signal-to-noise ratio of a small peak in this range is insufficient for the fitting. The wavelength range of the fitting is indicated by the thick gray lines at the abscissa of Figure 3. Although the peak at 500.15 nm consists of two transitions, the deviation of the pedestal shape from the single Voigt function is negligible.

From the fitting results, the magnetic field strength was evaluated from the peak wavelength difference between the ordinary and extraordinary spectral lines which mainly consist of the σ components. The line-integrated intensity, corresponding to the area of the Voigt profile, and electron density were measured as averaged values from the ordinary and extraordinary spectral lines. Typical results are shown in Figure 4. In the abscissa of the figure, we define y as the distance between the plasma center and the viewing chord. The positive and negative values indicate the upper and lower half of the plasma column, respectively. The position $y = 0$ was chosen at the peak of the Gaussian function fitted to the line-integrated intensity. The data measured on a viewing chord at the largest y was omitted because reproducibility for identical discharges was much worse than for the data measured on the other viewing chords. This is because the intensity is the lowest at the edge. The polarity of the magnetic field in Figure 4(a) indicates the field direction with respect to the observer; a direction from the observer to the plasma is positive. The magnetic field strengths evaluated independently from three spectral lines (i), (ii), and (iii) are consistent as can be seen in Figure 4(a). In particular, the result from spectrum (iii) has the smallest error bars (also see Figure 5) due to having the largest signal-to-noise ratio of the three lines. The error bar is about ± 10 mT near the center. It becomes larger at the edge accompanying the decrease in the intensity. After taking into account the wavelength calibration error, the total error bar is about ± 13 mT near the center. In Figure 4(c), $\overline{n_e}$ deduced from the Stark broadening is 10^{22-23} m^{-3} and consistent with previous measurements.[18]

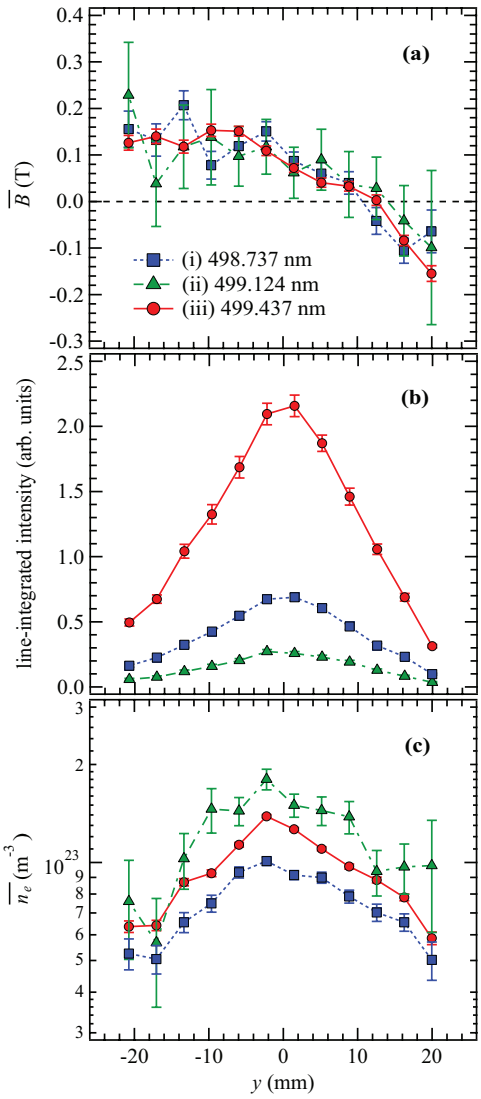

FIG. 4. Typical fitting results (#12970): (a) "apparent" magnetic field strength, (b) line-integrated intensity, and (c) electron density. The dotted line with filled squares denotes the result from spectral line (i), dashed-dotted line with filled triangles denotes (ii), and line with filled circles denotes (iii). The polarity of the magnetic field indicates the field direction with respect to the observer; a direction from the optical system to plasma is positive.

A. Evaluation of the vector magnetic field spatial profile

The analysis in this section uses data from spectral line (iii), the line with the best signal-to-noise ratio. In order to resolve the radial profiles of the magnetic field components, the experimental results $\overline{B}$ were fitted by a curve based on an inversion calculation. In the inversion calculation, the line-integrated spectral lines were synthesized from the presumed local magnetic field profile and the measured line-integrated emission intensity and $\overline{n_e}$ profiles. The local magnetic field profile was determined by least-squares fitting to the experimental results. The detailed calculation procedure is as follows:

1. The azimuthally symmetric vector magnetic field $\boldsymbol{B}$ can be expressed in a cylindrical coordinate system $\{r\phi z\}$ as

$$\boldsymbol{B} = \frac{1}{2\pi r}\left(-\frac{\partial\psi}{\partial z}, \mu_0 I, \frac{\partial\psi}{\partial r}\right), \tag{4}$$

where $\psi(r, z)$ is the poloidal flux, $I(r, z)$ is the current linked by a circle of radius r with center on the axis, and μ_0 is the vacuum permeability. Because the plasma under consideration is a long stretched jet, we assume uniformity in the z-direction so that $\partial\psi/\partial z \simeq \partial I/\partial z \simeq 0$. The poloidal and toroidal fields thus correspond to the z- and ϕ-components, respectively. The radial profiles of ψ and I are approximated by fourth-order polynomials

$$\psi(r) = C_2 r^2 + C_4 r^4, \tag{5}$$

$$I(r) = D_2 r^2 + D_4 r^4, \tag{6}$$

where the coefficients C_2, C_4, D_2, and D_4 are determined by least-squares fitting. No odd power of r is used because of mathematical regularity considerations as discussed in Ref. 19.

2. The line-integrated spectral line profiles along the viewing chord $\overline{P}(y;\lambda)$ are calculated as

$$\overline{P}(y;\lambda) = 4\int_{y-a_v}^{y+a_v}\left[b_v^2 - \frac{b_v^2}{a_v^2}(y'-y)^2\right]^{\frac{1}{2}} \times\left[\int_{y'}^{r_m}\epsilon(r)p(r;\lambda)\frac{r}{\sin\alpha\sqrt{r^2-y'^2}}dr\right]dy', \tag{7}$$

where a_v and b_v are the minor and major radii of the viewing spot, r_m is the maximum radius for the integration of the emission, $\epsilon(r)$ is the local intensity, $p(r;\lambda)$ is the local spectral line profile, and α is the angle between the viewing chord and the axis of the vacuum chamber. The radius of the center electrode 101.5 mm is used for r_m. By using the Jones calculus,[20] $p(r;\lambda)$ can be calculated as a function of the angle $\gamma(r)$ between the local magnetic field vector and viewing chord, the local magnetic field strength, and the local electron density as

$$\begin{aligned} p(r;\lambda) = {} & \left(\sin^2\gamma\right)L_{V\pi}(w_G, w_L, \lambda_0;\lambda) \\ & + \frac{1}{2}(\cos\gamma \pm 1)^2 L_{V\sigma^+}(w_G, w_L, \lambda_0 - \Delta\lambda_B;\lambda) \\ & + \frac{1}{2}(\cos\gamma \mp 1)^2 L_{V\sigma^-}(w_G, w_L, \lambda_0 + \Delta\lambda_B;\lambda), \end{aligned} \tag{8}$$

where the upper and lower signs correspond to the right- and left-circularly polarized spectra, respectively. The subscripts π, σ^+, and σ^- on the Voigt functions represent the π and $\sigma^\pm$ components and $\Delta\lambda_B(r)$ is the peak wavelength shift of the σ components by the Zeeman effect. Finite $\gamma(r)$ results in unfavorable mixing of the π and σ components that decreases the apparent magnitude of the Zeeman splitting. In the calculation, $w_G(r)$ is approximated to be constant over the whole emission region as mentioned before. $\epsilon(r)$ and $w_L(r)$ are evaluated from the measured line-integrated intensity and $\overline{n_e}$

TABLE II. Determined values of the coefficients in Eqs. (5) and (6).

$C_2 = 2.08 \pm 4.51 \times 10^{-1}$
$C_4 = -1.89 \times 10^{3} \pm 7.46 \times 10^{2}$
$D_2 = 1.37 \times 10^{7} \pm 6.81 \times 10^{6}$
$D_4 = 5.23 \times 10^{10} \pm 1.69 \times 10^{10}$

in Figure 4. These experimental data are fitted by the Gaussian functions. From the fitted curves, $\epsilon(r)$ is calculated by the Abel inversion[21] taking into account the effect of the finite viewing spot area. $w_L(r)$ is calculated assuming that the measured Stark broadening reflects the maximum electron density along the viewing chord, namely, $n_e(r) = \overline{n_e}(y = r)$. The instrumental function is included in w_G and w_L.

3. In the fitting procedure, first $\boldsymbol{B}(r)$ is calculated from $\psi(r)$ and $I(r)$ by Eq. (4). By using the calculated $\boldsymbol{B}(r)$, the coefficient in Table I, and a given viewing chord direction, $\Delta\lambda_B(r)$ and $\gamma(r)$ are then evaluated. Second, $\overline{P}(y;\lambda)$ is calculated by Eqs. (7) and (8) using $\Delta\lambda_B(r)$ and $\gamma(r)$, measured parameters $\epsilon(r)$ and α, and a given boundary condition r_m. Third, $\overline{B}(y)$ is evaluated from the peak wavelength shift of $\overline{P}(y;\lambda)$ by least-squares fitting of the Voigt function. Finally, the evaluated $\overline{B}(y)$ is least-squares fitted to the experimental data in Figure 4(a) with coefficients C_2, C_4, D_2, and D_4 in Eqs. (5) and (6) as fitting parameters. For the least-squares fittings, the Levenberg-Marquardt algorithm[22,23] was adopted. It is possible to determine both the ϕ- and z-components of the magnetic field at the same time since the former is an odd function and the latter is an even function of y.

The fitting result and determined magnetic field components are shown in Figures 5 and 6, respectively. Determined coefficients C_2, C_4, D_2, and D_4 are shown in Table II. In Figure 6, the evaluated field strength of the ϕ-component $|B_\phi|$ radially increases with increasing the enclosed current. The value is up to about 0.14 ± 0.04 T at $r = 20$ mm. $|B_z|$ is up to 0.66 ± 0.14 T on the axis and radially decreases to about 0.19 ± 0.24 T at $r = 20$ mm. The value of $|B_z|$ on the axis is significantly larger than the vacuum field, a poloidal field existing prior to the formation of the plasma, which has a uniform field strength of about 0.1 T[24] within the radial region considered.

In order to confirm the validity of the inversion procedure, a measurement under the reversed poloidal field was conducted. In this case the poloidal field is directed away from the gun electrodes in the vicinity of the chamber axis. A schematic illustration of $\boldsymbol{B}_\phi$ and $\boldsymbol{B}_z$ vectors with respect to the viewing direction in the regions where $y > 0$ and $y < 0$ is shown in Figure 7. The measured $\overline{B}$ is shown in Figure 5 by the diamonds. By using the radial profiles of B_ϕ and B_z determined from the normal poloidal field discharge, the $\overline{B}$ expected to be observed in the reversed field discharge was calculated. The calculated result is indicated by the dashed line in Figure 5. The experimental and calculated results are consistent.

We compared the evaluated magnetic field components with those measured by a B-dot magnetic probe array.[25] The

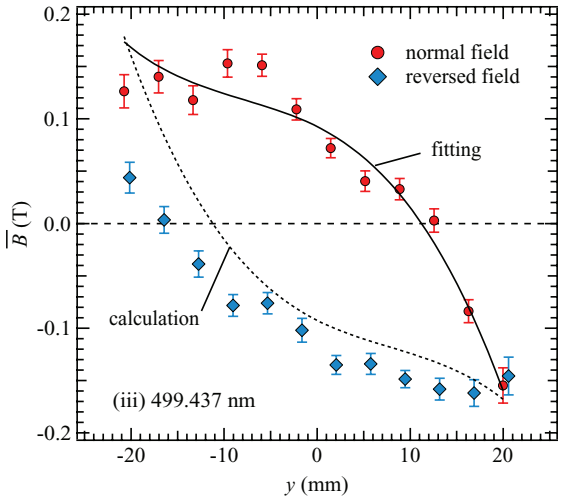

FIG. 5. Measured "apparent" magnetic field strengths from spectral line (iii) with the normal (#12970) and reversed (#13008) poloidal field directions. The line denotes the fitting result to the normal field data. The dashed line denotes the field-strength expected to be observed in a reversed field discharge; it is calculated by using the determined B_ϕ and B_z profiles in the normal field discharge plotted in Figure 6.

intrinsic issues of the magnetic probe diagnostic are its possibility of disturbing the plasma and the assumption that the magnetic field diffuses on the spatial scale of the probe radius. Although detailed investigation of these issues are outside the scope of the present work, comparison of the optical data obtained here to the probe data is useful to estimate the accuracy of the magnetic probe measurements. The magnetic probe array detects the three-dimensional field components at every 20 mm spatial position. The whole system is insulated from the plasma by an 8.4 mm outer diameter quartz tube. The time-averaged field strengths between 7 and 8 μs from the onset of the normal poloidal field discharge are plotted in Figure 6. As can be seen in the figure, the spectroscopy and magnetic probe results are in agreement within a factor of 3.

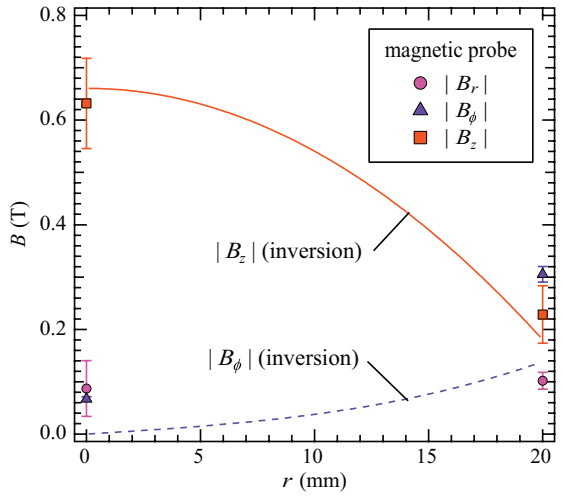

FIG. 6. Determined radial profiles of the magnetic field strengths. The dashed line represents $|B_\phi|$ and the line represents $|B_z|$. Markers: the filled circles, triangles, and squares, respectively, represent the r-, ϕ-, and z-components of the magnetic probe data (#12758).

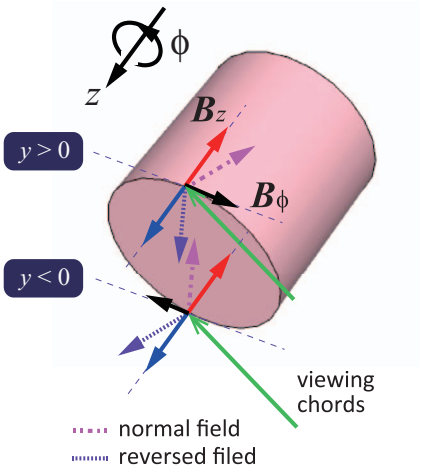

FIG. 7. A schematic drawing of $\boldsymbol{B}_\phi$ and $\boldsymbol{B}_z$ vectors and viewing chord in the regions $y > 0$ and $y < 0$ for the normal and reversed poloidal field discharges.

A possible interpretation for the agreement is diffusion of the magnetic field into the probe. The magnetic Reynolds number is defined as $R_M = \mu_0 LU/\eta_\perp$, where L is the characteristic spatial scale, U is the velocity, and $\eta_\perp$ is the resistivity in the direction perpendicular to the magnetic field. In the spatial scale of the magnetic probe, $R_M = 1.4$ with $L = 4.2$ mm , $U = 30$ km/s,[18] and $\eta_\perp = 1.1 \times 10^{-4}$ Ωm.[26] $\eta_\perp$ is evaluated with $T_e = 3$ eV and $n_e = 1.5 \times 10^{23}$ m^{-3}. This suggests that the magnetic field could be diffusive on the spatial scale of the probe. Meanwhile $R_M = 34 \gg 1$ with $L = 100$ mm. This indicates that the magnetic flux is frozen into the plasma in the spatial scale of the plasma jet. The fact that $|B_z|$ is significantly larger than the vacuum field strength supports this conclusion.

V. SUMMARY

A non-perturbing spectroscopic diagnostic of the magnetic field has been developed to measure the magnetic field profile in the Caltech coaxial magnetized plasma gun experiment. With the aid of a newly implemented polarization separating optical system, we have succeeded to detect the small Zeeman splittings in NII spectral lines with an accuracy of about ±13 mT. The local magnetic field components were resolved by comparing the experimental data with a synthetic calculation of line-integrated spectral lines. The estimated poloidal field strength was much stronger than the vacuum field existing prior to the formation of the plasma. This result supports the notion that the jet contains frozen-in stretched and squeezed-together poloidal field lines. The estimated field components were in agreement with the magnetic probe data.

ACKNOWLEDGMENTS

One of the authors (T.S.) acknowledges A. L. Moser, V. H. Chaplin, X. Zhai, and D. Felt for their technical assistance. This work was supported by U.S. DOE, NSF, and JSPS Institutional Program for Young Researcher Overseas Visits (Program for Educating and Cultivating International and Transdisciplinary Academians for Mechanical Engineering Education and Research) and Grant-in-Aid for Young Scientist (B) No. 24740367.

[1]P. M. Bellan, D. Kumar, E. V. Stenson, S. K. P. Tripathi, G. S. Yun, and A. L. Moser, AIP Conf. Proc. **1242**, 156 (2010).
[2]S. C. Hsu and P. M. Bellan, Phys. Plasmas **12**, 032103 (2005).
[3]F. C. Jahoda, F. L. Ribe, and G. A. Sawyer, Phys. Rev. **131**, 24 (1963).
[4]N. J. Peacock and B. A. Norton, Phys. Rev. A **11**, 2142 (1975).
[5]U. Feldman, J. F. Seely, N. R. Sheeley, Jr., S. Suckewer, and A. M. Title, J. Appl. Phys. **56**, 2512 (1984).
[6]J. F. Seely, U. Feldman, N. R. Sheeley, Jr., S. Suckewer, and A. M. Title, Rev. Sci. Instrum. **56**, 855 (1985).
[7]R. P. Golingo, U. Shumlak, and D. J. Den Hartog, Rev. Sci. Instrum. **81**, 126104 (2010).
[8]S. Mar, J. A. Aparicio, M. I. de la Rosa, J. A. del Val, M. A. Gigosos, V. R. González, and C. Pérez, J. Phys. B **33**, 1169 (2000).
[9]B. H. Bransden and C. J. Joachain, *Physics of Atoms and Molecules*, 2nd ed. (Pearson Education, 2003), Chap. 6.
[10]M. Goto, in *Plasma Polarization Spectroscopy*, edited by T.Fujimoto and A.Iwamae (Springer, 2008), pp. 13–28.
[11]T. Shikama, S. Kado, H. Zushi, M. Sakamoto, A. Iwamae, and S. Tanaka, Plasma Phys. Controlled Fusion **48**, 1125 (2006).
[12]J. B. Green and H. N. Maxwell, Phys. Rev. **51**, 243 (1937).
[13]C. C. Kiess, Science **107**, 649 (1948).
[14]*NIST Atomic Spectra Database*, Version 4.
[15]G. T. Best, Appl. Opt. **12**, 1751 (1973).
[16]S. You, G. S. Yun, and P. M. Bellan, Phys. Rev. Lett. **95**, 045002 (2005).
[17]D. Kumar, A. L. Moser, and P. M. Bellan, IEEE Trans. Plasma Sci. **38**, 47 (2010).
[18]G. S. Yun and P. M. Bellan, Phys. Plasmas **17**, 062108 (2010).
[19]H. R. Lewis and P. M. Bellan, J. Math. Phys. **31**, 2592 (1990).
[20]D. S. Kliger, J. W. Lewis, and C. E. Randall, *Polarized Light in Optics and Spectroscopy* (Academic, 1990), Chap. 4.
[21]I. H. Hutchinson, *Principles of Plasma Diagnostics*, 2nd ed. (Cambridge University Press, 2002), pp. 141–144.
[22]K. Levenberg, Q. Appl. Math. **2**, 164 (1944).
[23]D. W. Marquardt, SIAM J. Appl. Math. **11**, 431 (1963).
[24]G. S. Yun, Ph.D. dissertation, California Institute of Technology, 2008, pp. 20–22, see http://thesis.library.caltech.edu/2979/.
[25]C. A. Romero-Talamás, P. M. Bellan, and S. C. Hsu, Rev. Sci. Instrum. **75**, 2664 (2004).
[26]F. F. Chen, *Plasma Physics and Controlled Fusion*, 2nd ed. (Plenum, 1984), p. 183.